

Microfluidic Salt Precipitation: Implications for Geological CO₂ Storage †

Tsai-Hsing Martin Ho and Peichun Amy Tsai*

Salt precipitation in porous media can detrimentally hinder the processes of Carbon Capture and Storage (CCS) in deep saline aquifers because pore-blocking salt-crystals can decrease the injectivity of wells and formation permeabilities. It is, however, challenging to unravel the pore-scale dynamics and underlying mechanisms of salt nucleation using the conventional core-flooding techniques. Here, we conduct microfluidic experiments to reveal the high-resolution, pore-scale measurements of the de-wetting patterns and drying rate of brine and subsequent salt precipitation during gas injection. We investigate the effects of pore-structures and brine concentrations. The results show three distinct stages: (I) initial, (II) rapid growth, and (III) final phases, in the progression of salt nucleation with different rates and size distributions upon brine drying. Two types of crystal patterns, bulk crystal and polycrystalline aggregate, are observed. In addition, most of the large salt deposits ($\geq 0.5 \times 10^5 \mu\text{m}^2$) are precipitated at the near outlet region during the second rapid growth stage. The influence of porosity is demonstrated by correlating the brine-drying and salt-precipitation speeds during the second rapid growth phase.

1 Introduction

The carbon capture and sequestration (CCS) technology in deep saline formations is one of the most promising methods to mitigate the anthropological emission of CO₂ due to the ample storage capacity of saline aquifers.^{1–7} Salt, particularly Halite, precipitation may impede the CCS process and efficiency in deep saline formations, by blocking pore spaces⁸ and, in turn, decreasing the permeabilities of the formations.^{9–12} Such alterations and decrease of rock pores can detrimentally affect the injectivity, sealing, and storage capacity of the saline formations for the CCS technology.^{10–13}

To evaluate the influence of salt precipitation during CO₂ injection in the CCS process, the core-flooding method with CT (computed tomography) scans has been often used, by measuring the distributions of salt deposits, the change of pore-size, and the possible impairment of the rock permeability.^{14–23} Two common types of nucleated salt patterns have been observed experimentally: homogeneous and local salt precipitations. On the one hand, the homogeneous nucleation has a minor effect on the rock formation due to sufficiently-connected pore-space remained after the salt deposits.²¹ On the other, local salt precipitation can be a massive salt accumulation at the near-inlet regime of core samples.^{19,20} Some numerical studies have also revealed the dense deposits locally at near-wellbore region, leading to a reduction of the injectivity and a build-up of the injection pressure.^{15,23} More recently, several studies have been carried out to investigate the effects of injection rate,^{14,15,17,18} salinity,^{15,17} and temperature²³ on the salt precipitation.

Besides the conventional core-flooding experiments, microfluidics is another useful approach by providing pore-scale observations and insights of salt precipitation at micro/nano-scale. With various microfabrication methods, microfluidics allows direct visualization and quantitative measurements of multiphase flow and dynamics in a well-defined (patterned or random) microstructures.^{24–30} Recent microfluidic experiments mimicking the CCS process have identified that salt precipitation is composed of two different crystal configurations: bulk crystals and polycrystalline aggregates. Salt aggregates tend to grow around the bulk crystals and extend to a large range.²⁵ R. Miri et al. proposed a self-enhancing mechanism to explain the poly-crystal aggregation process, in which a liquid film exists and plays a critical role by connecting residual brine pools and drying front. The liquid film delivers salt ions to support the growth of salt aggregates.²⁷ The significance of water film is also mentioned by A. Rufai and J. Crawshaw, who reported a decrease of permeability in the water-wet channel, whereas no noticeable permeability change in the oil-wet channel.²⁹ In addition, M. Nooraiepour et al. injected different states of CO₂ (gas, liquid, or supercritical) into a vessel made of organic-rich shale rock that simulates the fractures of caprock. From their measurements, gas CO₂ results in the most extensive salt coverage compared to those for the liquid and the supercritical state of CO₂ injected.³⁰

Albeit these previous pioneering investigations of obtaining insights into salt precipitation at the pore scales, due to complex multiphase processes and interactions, quantitative pore-scale measurements of (i) salt distributions varying with brine-drying rate and (ii) the dependence of salt growing rate on the “in-situ” brine drying rate are still missing. To fill the knowledge gaps, in this work, we quantitatively elucidate the pore-scale dynamics of both salt precipitation and de-wetting patterns of brine in a well-defined porous network during continuous gas injection. By

Department of Mechanical Engineering, University of Alberta, Edmonton, Alberta, Canada T6G 1H9. E-mail: peichun.amy.tsai@ualberta.ca

† Electronic Supplementary Information (ESI) available: the microfluidic patterns, microfabrication processes, the methods of post-image analysis, and a supporting video are provided. See DOI: 00.0000/00000000.

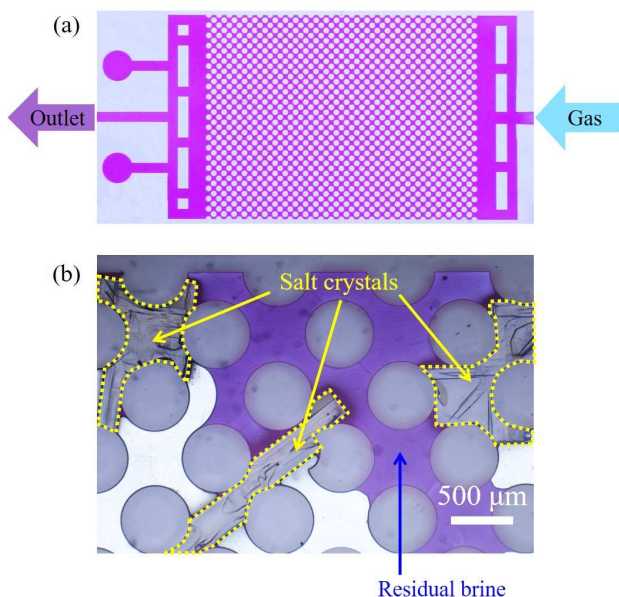


Fig. 1 Snapshots of our microfluidic experiments: (a) The microfluidic chip is initially saturated with a dyed salt solution. The brine is displaced by air (injected from right to left) at a rate of $500 \text{ } (\mu\text{l}/\text{min})$ at room temperature and 1 atm. (b) Precipitated salt crystals (indicated by the yellow dashed lines) nucleated in a residual brine pool (shown by the mauve color). As gas was continuously injected, salt concentration gradually exceeded the saturation point because of water evaporation, leading to more salt precipitation.

applying a series of post-image processes, we extract quantitative data and correlate the brine-evaporation and salt-nucleation rates at the pore-scale. We further analyze the distributions and morphologies of the salt precipitation changing with time and discuss the underlying mechanisms. Finally, we also investigate the effect of porosity on the dynamics of both brine drying and salt precipitation that mimic the CCS processes in a deep saline formation at pore-scales.

2 Materials and Methods

2.1 Microfluidics

The microfluidic device consists of an elastomer substrate covered by a thin transparent cover glass for clear visualization (see Fig. 1a). We fabricated the substrate using a replica molding method with Polydimethylsiloxane (PDMS) to create a well-defined porous structure³¹. In the replica-molding method, we first designed and fabricated the mold master by applying the standard deep reactive ion etching procedures (DRIE). PDMS elastomer was cast on the mold to form the microstructures and subsequently bonded with a microscope cover-slide for better sealing and observation. Two patterns of different porosity values, $\phi = 0.52$ and $\phi = 0.23$, are designed and used. Regular circular pillars (of the diameter of $d = 550 \text{ } \mu\text{m}$) are arranged in a body-centered lattice to form the porous pattern for $\phi = 0.52$. The $\phi = 0.23$ pattern is formed by micro-pillars (of the diameter of $d = 460 \text{ } \mu\text{m}$) in a hexagonal lattice. The pillar height (h) is fixed to be $h = 25 \text{ } \mu\text{m}$. The details of the DRIE procedures, replica-

molding processes, and microfluidic patterns (with images) are described in the Electronic Supplementary Information (ESI) †.

2.2 Experimental Section

We experimentally investigate the pore-scale dynamics of fluid transport and salt precipitation when air is injected in a porous medium initially saturated with brine. After air displaces brine, water molecules in the residual brine gradually evaporated. Subsequently, salt started to precipitate due to the supersaturation of salt as evaporation goes on. Fig. 1 shows representative snapshots of our microfluidic experiment in a porous network, initially fully saturated with brine in (a) and salt crystals precipitated at a later time in the residual brine in (b).

Three initial brine concentrations were used: 16.5%, 21.6%, and 25.6% (in weight fraction of NaCl in 100 ml DI water). Potassium permanganate (KMnO_4 , 1wt%) was added as a purple dye for better visualization and to conveniently and accurately measure the brine drying rate. We also tested the experiments without the additive dye but would need to manually analyze the data of brine-drying and salt-precipitation areas varying in time. We found consistent results of salt precipitation rates and morphologies of a NaCl solution without and with KMnO_4 , although the latter may contribute to more poly-crystalline and feather-shaped precipitations as well as a maximal error of 5% for the total amount of salt crystallization, which corresponding to a maximal error of $\approx 5 \times 10^{-3}\%$ for the growth-rate (per second). For each concentration, a new microfluidic device was initially placed in a vacuumed chamber to saturate with a brine solution fully. The ambient air (with $\approx 16\%$ relative humidity) was injected by a syringe pump (Chemyx Inc. Fusion 6000) at a constant rate of $500 \text{ } (\mu\text{l}/\text{min})$ at room temperature (22°C), and the microfluidic outlet is open to 1 atm. A digital camera (Canon EOS 70D) was used with a LED backlighting to capture the dynamics of water drying and salt precipitation (at a rate of one frame per 60 secs for 9 hours to record a set of a complete experiment).

2.3 Image Analysis

To accurately quantify the brine-drying and salt-nucleation dynamics, we performed a series of post image processes of the captured snapshots to distinguish and analyze the changes of the three phases (e.g., gas, liquid, and solid) involved. As shown in Fig. 1b, the solid salt crystal gradually nucleated after the injected air drains the residual brine. Our image analysis can differentiate the time-evolution of the coverage areas (or volumes) of remaining brine and salt nucleation. To precisely identify the boundaries of the porous structure, residual brine, trapped air, and nucleated salts, the recorded image sequences were processed via a color threshold algorithm using ImageJ (NIH Image).³² For a better result, the CIELAB color space (L^* , a^* , and b^*) was used as the thresholding color space. This color space includes all perceivable colors, which allows us to differentiate the minor color difference between the boundaries of salt crystals and the PDMS substrate. We also minimize the background light deviation between each image by adjusting the desirable range of brightness.³³

From each series of experimental images recorded, we finally

generated two binary image sequences displaying (i) the drying process of residual brine and (ii) nucleation process of salt crystals. By measuring coverage areas of these two binary-image sequences, i.e., $A_B(t)$ and $A_C(t)$ for the brine residual and the salt nucleation areas varying with time (t), respectively, we were able to calculate several relevant time-evolving results accurately. Because our microfluidic porous network has a uniformed height ($h = 25 \mu\text{m}$), the (volumetric) brine drying rate will be $\dot{V}_{\text{brine}} = |h \cdot (dA_B/dt)|$. Similarly, by assuming the salt crystallizations occupy the entire channel height, h , the (volumetric) growing rate of the salt precipitation is $\dot{V}_{\text{salt}} = h \cdot (dA_C/dt)$. We hence carried out linear fits of $dA_B(t)/dt$ and $dA_C(t)/dt$ to accurately calculate the the drying rate of residual brine and the nucleation growth rate of salt crystals, respectively, for the different drying periods. These are critical for further analyzing the salt precipitation dynamics at the pore-scale. The thresholding setting and image calibration are described in Section 3 of ESI †.

3 Results and discussion

3.1 Brine Drying and Salt Precipitation

Fig. 2 reveals the general dynamics of (i) de-wetting and drying of brine as well as (ii) salt precipitation in the microfluidic porous medium. Shown in Fig. 2a are the typical experimental snapshots, revealing the sequential processes of initial brine drainage, subsequent drying, and later-time salt precipitation, under a constant injection of air. These processes, occurring at different timescales, are revealed by the initial, rapid-drainage of brine (with fast-decreasing purple area in Fig. 2a), subsequent slow-change of brine coverage (e.g., at 30%–50% drying time in Fig. 2a) and slow salt nucleation (shown by the appearance and accumulation of black spots between 30%–100% of drying time in Fig. 2a), respectively. By quantitative image analysis of the time-varying coverage area (e.g., Fig. 2a snapshots), we measured the initial brine-drainage, subsequent drying, and final salt-precipitation rates, as shown in Fig. 2b, to elucidate the corresponding dynamics and mechanisms at different times.

From inspections of sequential snapshots and quantitative measurement (e.g., 2a and b, respectively), we observe three sequential states of brine de-wetting: initially full-saturation, drainage, and drying of residual brine. More specifically, the microfluidic observations generally show that, in the first half-hour of air-injection, the brine solution in the pore structure remained fully-saturated because the gas pressure needs to overcome the capillary pressure when displacing water at the pores.³⁴ This period corresponds to the initial steady, constant plateau region of normalized residual brine volume, shown by the Fig. 2b initial data (▼) between a dimensionless time, $t^* = -0.2$ and 0. Here, the dimensionless time (t^*) is defined as $t^* = (t - t_o)/(t_f - t_o)$, where t_o is the initial time of drainage, and t_f is the complete drying time.

Once the pressure is greater than the capillary pressure, injected air starts to expel brine quickly and, hence, dramatically reduces the brine saturation in the porous network. This drainage state is illustrated by the steep decrease in the volume of residual brine displaced (see Fig. 2b data (▼) for $0 < t^* \lesssim 0.1$). After air drains the majority of brine, the residual brine is nearly immobile

and trapped in some areas of the pores, forming several pools of residual brine of various sizes. Because the injected air is unsaturated with water vapor (about 16% of relative humidity), water molecules keep evaporating from these brine patches to the surrounding air. The evaporating stage shows three slightly different trends of drying rates, revealed by the blue curve right after the sharp drop of the drainage phase.

The dynamics of salt nucleation is simultaneously measured and shown by the increasing area of salt crystals in time, depicted by (◆) in Fig. 2(b). The data presented is for the case of 16.7wt% initial salt concentration and $\phi = 0.52$. We observe three phases of salt precipitation and categorized them into: (I) *initial*, (II) *rapid growth*, and (III) *final* stages, based on the different nucleation growth rates observed. We also observed that the faster drying period of residual brine corresponds to a more rapid precipitation of salt. Measurement in Fig. 2(b) reveals the salt nucleation at the initial stage (I) grows at a rate of 0.6 (unit pore size/ t^*) while under a slower drying rate of residual brine of 210 (unit pore size/ t^*). Subsequently, the nucleation growth rate at the rapid growth stage (II) accelerates up to 172.8 (unit pore size/ t^*) with the corresponding highest drying rate of 450 (unit pore size/ t^*). At the final stage (III), nucleation growth tends to slow down to a rate of 51.8 (unit pore size/ t^*) as the drying rate of brine decreases to a smaller rate of 170 (unit pore size/ t^*) before completely drying out. We conducted three independent experiments for each salt concentration for the two porosity cases, and in total 18 sets of experimental data were analyzed. For all the concentration and porosity cases, three distinct salt growing regimes as described above are observed, as shown in Fig. S5 in ESI †.

To further illustrate the correlation between the nucleation rate and drying rate at different stages, we propose the following possible mechanisms. In the initial phase, the residual brine is confined in the throat (or neck) of pillars by capillary force, i.e., the narrowest gap of pore structure. The evaporation rate, therefore, stays low because of the limiting contact area between gas and liquid. Salt nucleation at this early stage mainly occurs in the small residual brine area (trapped in the throat). Due to this limiting size of the brine area, the coverage of nucleated salt grows slowly.

As water further evaporates, the salt concentration of large brine pools, occupying more than 20 pore units in Fig. 2 gradually exceeds the solubility limit to initiate the rapid growth of salt nucleation. This fast process is shown in the second (II) rapid growth region (in the light blue shaded area) in Fig. 2b. Two following mechanisms are observed and likely cause this significant increase in the nucleation rate. First, the gas-liquid contact front gradually shifts from the throat towards the region with bigger pore space, which enlarges the gas-liquid contact area and, in turn, accelerates water evaporation and salt nucleation. Second, the small salt deposits, nucleated at the initial stage, can help to speed up the evaporation and nucleation processes at the same time by creating a positive feedback loop discussed below.

The hydrophilic nature of salt crystals can play a crucial role in initiating this feedback loop by attracting the surrounding brine to form a thin film on the crystal surfaces.¹² This affixed brine film largely increases the gas-liquid contact area and enhances

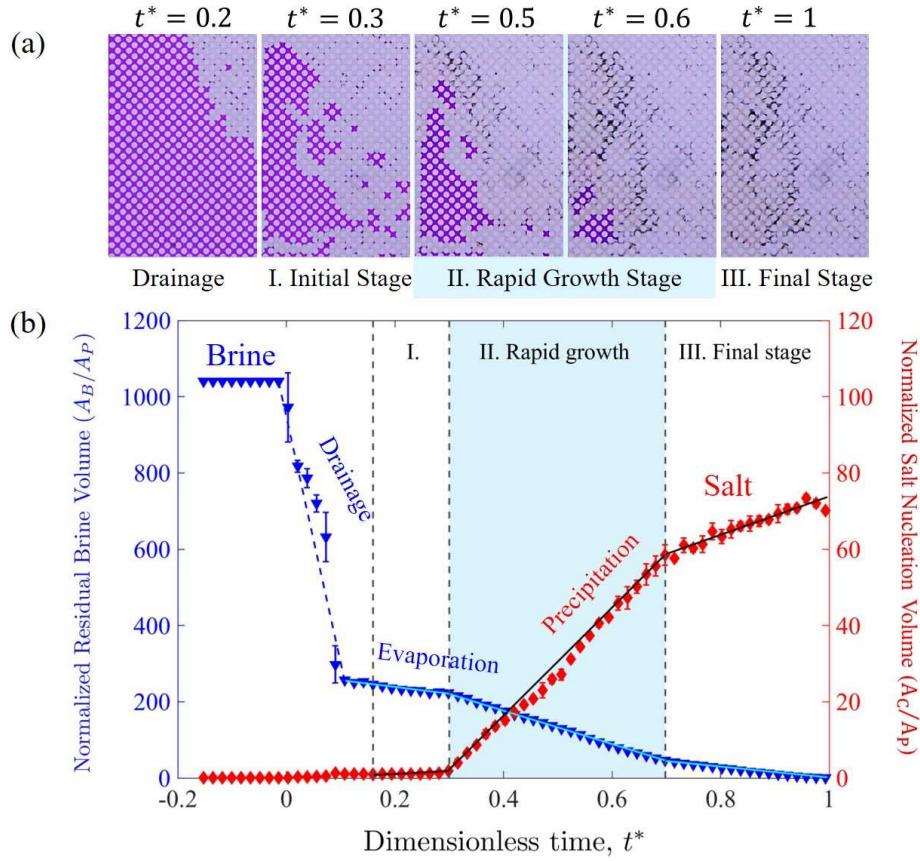


Fig. 2 (Supporting movie †) Simultaneous dynamics of both brine drainage/drying (▼) and salt nucleation (◆) in a well-defined microfluidic network of a constant depth, under a constant air injection (with 16.7% w/w initial salt concentration). (a) Representative experimental snapshots of salt precipitation during a brine drainage. The dimensionless time (t^*) represents a characteristic time with the definition of $t^* = (t - t_o)/(t_f - t_o)$, where t_o is the initial time of drainage, and t_f is the final time when the brine is dried completely ($t_o = 2760$ s and $t_f = 20,040$ s in this case). (b) The changes of residual brine (▼) and salt nucleation (◆) volumes in time; here the dimensionless volume is normalized by the unit volume of the regular pore-structure (with a constant depth), i.e., in terms of the numbers of unit-pore. From (b), the development of salt nucleation reveals three distinct phases: (I) initial slow, (II) rapid growth, and (III) final stages characterized by different growth rates measured. Here, A_B represents data of residual brine area varying in time; A_C means the area of salt precipitation; A_P is a constant of a unit pore area we defined ($A_P = 2.51 \times 10^5 \mu\text{m}^2$ in this case; see ESI † for the details regarding A_P).

water evaporation. Meanwhile, a new layer of salt crystal nucleates on the original crystal surfaces after water escapes from the brine film, and it extends the coverage of salt precipitation. This newly formed salt creates a more brine-film covered area. It further promotes the positive feedback loop, thereby enhancing further nucleation. Large brine pools adjacent to the drying and nucleation interfaces are the major ions sources in this rapid growth stage. They continuously provide sufficient salt ions to the nucleation region and keep the salt precipitation growing by capillary forces supplying with the ionic current. As a result, the majority of residual brine is consumed and large salt precipitate in this stage.

The final stage of salt nucleation occurs when most of the large brine pools are completely dried, and the majority of salt ions in the system is consumed. The growing rate of salt nucleation thus becomes slower due to the salt concentration in the remaining brine being too low to keep in a supersaturation state, as shown in the final region III in Fig. 2b. It hence takes time to regain the supersaturation condition and continues to nucleate the rest

of salt ions before the system is completely dried out.

3.2 Pore-scale Salt Precipitation

We observed two primary types of salt morphology from the images of final drying patterns under a microscope: large bulk crystals and polycrystalline aggregates. These observations are in agreement with previous microfluidic studies.^{25,27} Large bulk crystals, with transparent and ordered cubic structure, nucleate first via the self-assembly process of salt ions in the liquid phase when the ion concentration exceeds the solubility in certain thermodynamic conditions.³⁵ After the appearance of bulk crystals, polycrystalline aggregates nucleate on the gas-liquid-solid interfaces and further grow into a group of disordered salt crystals, when a sufficient ion supply is received from the brine sources.³⁶ The assemblies of bulk crystals and polycrystalline aggregates are revealed in all three nucleation stages, illustrated in Fig. 3. For each phase, each row of image sequences demonstrates the evolution of salt nucleation before and after the appearance of the precipitant as well as the zoom-in microscopic images, using $5 \times$

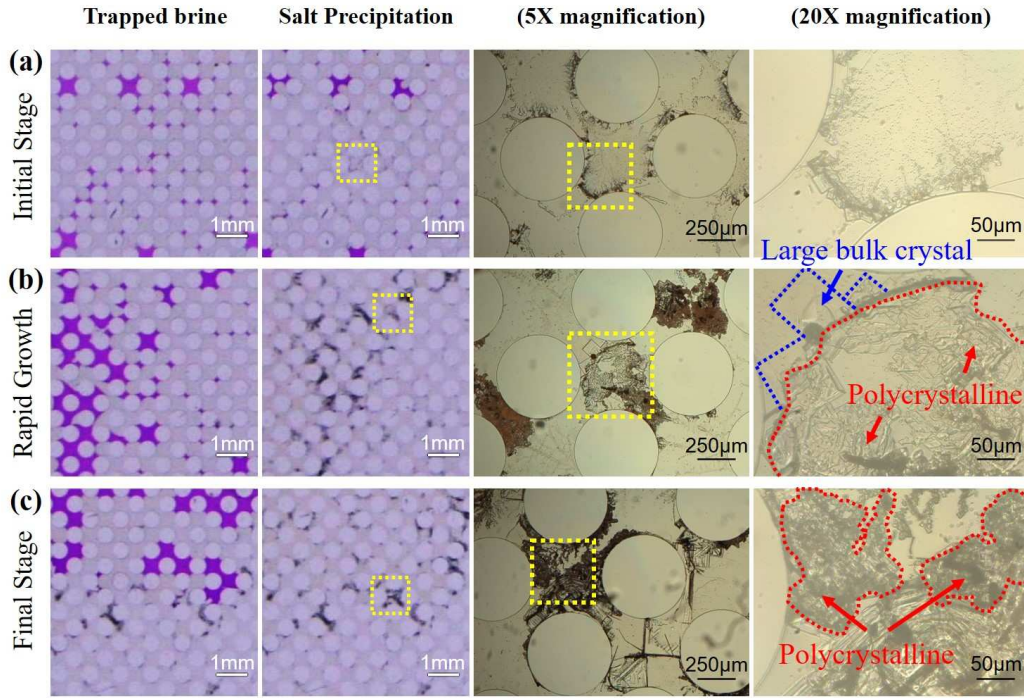


Fig. 3 Morphologies and patterns of the salt nucleation at the different nucleation stages. Each row of image sequence reveals the development of salt nucleation with the initial residual brine area, subsequent salt precipitation patterns, and magnified salt morphologies under $5\times$ and $20\times$ magnifications at different nucleation stages: (a) initial stage, (b) rapid growth stage and (c) final stage, which are delineated by the different crystallization speeds measured in Fig. 2b.

and $20\times$ magnifications.

At the initial stage (I), the majority of salt crystals first appear inside the small brine spot (≈ 1 pore space), trapped within the throat of the pore space. As the shrinkage of small drying brine spots, a few salt crystal branches nucleate and extend from the gas-liquid interface towards the air region to construct the backbone structure for the *polycrystalline* aggregates. Because of the limiting ion supply from these brine spots, these backbone structures stop growing and deposit in the form of tiny salt debris, as shown in the image sequence in Fig. 3a.

During the rapid growth stage (II), large brine pools provide sufficient salt ions to assemble bigger bulk crystals. Thus, the poly-crystalline backbones further developed to create the dendritic (or feather-like) frameworks inside the pore area, as shown in Fig. 3b. The dendritic structure helps to increase the contact area between the air and brine by forming a thin brine film via a capillary effect. The brine film can further transport ions from other brine patches. With more salt ions participate in constructing the poly-crystal, dendritic salts start to connect and merge. They generate a much larger and more complicated salt aggregate, which gradually fills the pore space, as shown in the $20\times$ magnification of image sequence Fig. 3b. This self-enhancing process can, therefore, precipitate a large salt crystal assembly, also shown in Fig. 4a, in the pores before completely drying out.

In the final stage (III), salt ions in the rest of brine pools continue migrating to the vast precipitation region and nucleating on the surface of salt aggregates because of the strong capillary induced flow. The hydrophilic nature of salt crystals also helps to

keep these delivered ions on the crystal surface. It makes the whole aggregate structure more complicated, as shown in the $20\times$ magnification of image sequence Fig. 3c.

3.3 Global Distribution of Salt Precipitation

Fig. 4a shows the final distribution of salt precipitation after the porous structure was completely dried. A large amount of salt accumulates locally at the position close to the outlet channel to form banded salt deposits, as highlighted by the yellow dash line. This banded precipitation can block accessible pathways for the injecting gas and can potentially damage the pore structure. How to explain the appearance of this massive local salt accumulation? We first noticed that the distribution of salt precipitation strongly depends on the initial location of residual brine. Large brine pools are trapped in the area close to the outlet channel. In contrast, the remaining brine of small and medium-size widely distributes around the region close to the injection channel after the majority of brine was drained by gas.

Fig. 4b shows the size-distribution of the salt deposits precipitated in the three nucleation stages. The bottom x-axis represents the size of salt nucleation in the unit of micron squares (μm^2), while the top axis is the number of pore spaces (being occupied by salt). From this statistic result of the salt distribution, about 75% of salt is nucleated during the (II) rapid growth stage. Most salt (more than 64%) that is precipitated in the initial stage (I) is smaller than $\approx 500 \mu m^2$ (i.e., $\approx 0.2\%$ of A_p). These small salt deposits mostly scatter around the near-inlet region but have little impact on the pore connectivity. In contrast, the salt aggregates

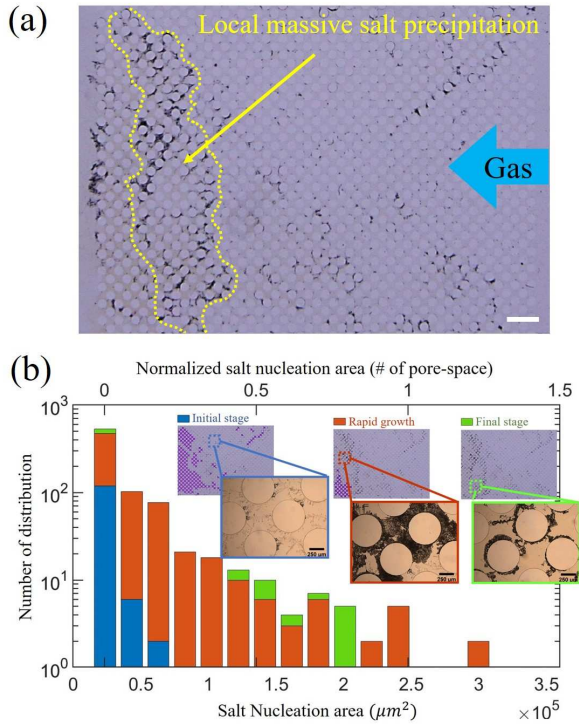


Fig. 4 The spatial and size distributions of salt precipitation for the case of $\phi = 0.52$. (a) A snapshot of salt distribution after the porous system was completely dry. The scale bar represents 2 mm. (b) Statistical analysis of the size distribution of salt precipitations nucleated at the different stages: I, II, III, shown by the bars of ■, ■, ■, respectively. This distribution diagram presents the numbers of salt-nucleation spots of particular sizes, in μm^2 (in the bottom axis) and by the numbers of unit pore size of $A_p = 2.51 \times 10^5 \mu\text{m}^2$ (in the top axis).

of a size larger than $0.5 \times 10^5 \mu\text{m}^2$, occupying $\approx 20\%$ of A_p , are all jamming at the region close to the outlets of the channel to form the banded salt deposits as mentioned in Fig. 4a. This massive local precipitation can likely block the pathway of air flow that may potentially reduce the permeability of porous medium and affect the injectivity.

3.4 Development of Extended Salt Precipitation

Shown in Fig. 5 are representative sequential snapshots demonstrating how a massive salt precipitation develops locally during the rapid growth stage (II). Initially, a few salt deposits have been precipitated near the large residual brine pools in the initial stage (I). The leftover brine was observed to shrink in the direction pointed by the blue arrows in Fig. 5a. With the brine shrinkage, the pore area, shown by the blue dashed rectangular in Fig. 5b, in front of the brine pool turns to the color of lighter purple, indicating the brine liquid moving from the original pore space to the salt-covered region. Simultaneously, more salt precipitates and further extends the coverage shown in the red rectangular in Fig. 5c. This process is consistent with the self-enhancing mechanisms proposed by the previous studies^{12,27} and discussed above. The hydrophilic nature of salt sustains a brine film on the surfaces of salt aggregate, which helps deliver the residual brine pools to the areas of precipitated salt (see Fig 5d). As water keeps evap-

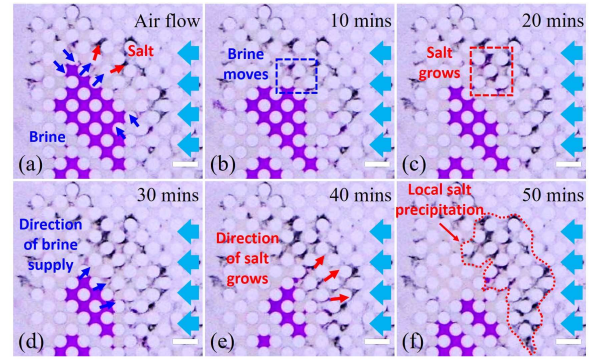


Fig. 5 (Supporting Movie) Development of local salt precipitation in the rapid growing regime (II). The representative image sequences are taken about 4 hours after air injection, with 10 minutes time lapse. Blue arrows indicate the flow direction of the brine, attracted by nucleated salt. Red arrows show the growing direction of salt aggregate, which attracts the fresh brine. The air flow goes from the right hand side. The scale bars represent 1 mm. A supporting movie is given in the ESI †.

orating from the brine film, fresh brine is provided from the pool to the drying surface to dilute the salt concentration, as in Fig 5e. As a result, more salt ions transport to the drying area and enhance the growth of the salt aggregates to become massive salt precipitation (see Fig 5f).

3.5 Effect of Porosity

The porosity not only is a key parameter measuring the permeability of the porous structure^{34,37} but also influences the competition between viscous and capillary forces on a multi-phase interface.^{34,38} Porosity, hence, can affect the transport of salt ions, which directly affects the rates of water evaporation and nucleation growth. As a major objective, here we investigate the influence of porosity on the distribution and size of salt precipitation. By comparing the microfluidic observations obtained from two porosity cases ($\phi = 0.52$ and $\phi = 0.23$), we observed that, under the same conditions of air injection (of $500 \mu\text{l}/\text{min}$), the cases of $\phi = 0.23$ require $\approx 20\%$ more time to initiate the drainage process than that of $\phi = 0.52$, because of a greater local capillary pressure to be overcome due to the low permeability (or porosity).

Fig. 6 reveals the correlation between the (areal) growing rate of salt nucleation (i.e., \dot{V}_{salt}/h) and the (areal) drying rate of residual brine (i.e., \dot{V}_{brine}/h) in the rapid growth stage (II) for three different initial salt concentrations, as the microfluidic gap (h) is kept constant. The dashed lines in Fig. 6 represent the fitting curves of linear regression, based on a least-squares fit. Detailedly, we carried out a fitting of simple linear regression of a functional form of $Y = aX + b + \epsilon$, where Y is the dependent (or responsive) variable (e.g., areal salt growing rate for Fig. 6), X is the independent (or input) variable (e.g., areal brine drying rate for Fig. 6), ϵ represents the error or residual. The fitting results explicitly describes a relationship between the response and input variables, with approximately a linear relationship. The fitting results also illustrate the positive correlation between salt precipitation and the evaporation of brine rates, with a constant and positive slope. More specifically, the slopes of the fitting lines are

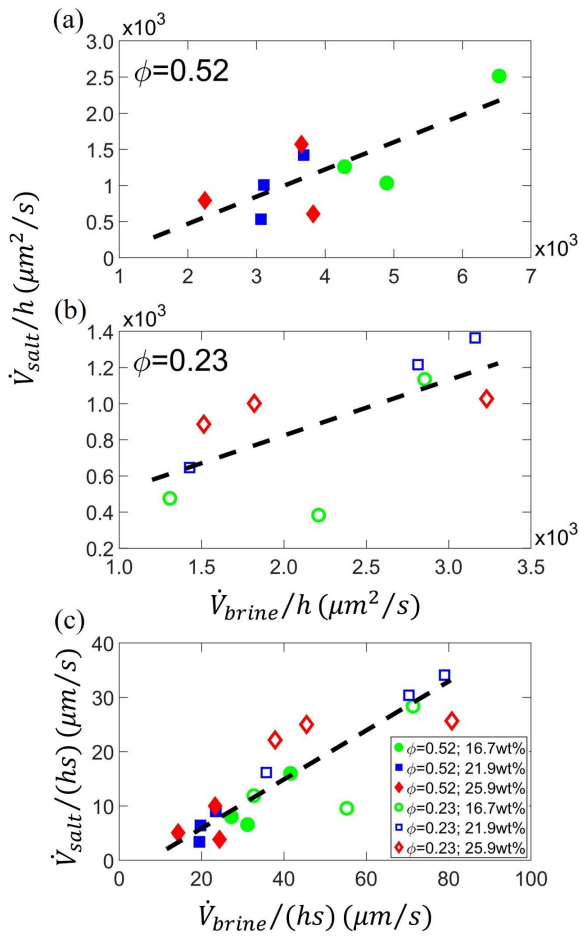


Fig. 6 Correlations between the growth rate of salt nucleation and drying-rate of the residual brine in the (II) rapid growth phase of nucleation, for $\phi = 0.52$ and $\phi = 0.23$ in (a) and (b), respectively. Here, \dot{V}_{salt} and \dot{V}_{brine} represent the volumetric salt growing rate and brine drying rate, respectively; h ($= 25 \mu\text{m}$) is the uniform depth of the porous structures. (c) Data collapse of a new correlation of the data in (a) and (b) divided by the interspacing distance, s . The dashed lines represent best fitting results based on the (least-squares residual) linear fit for the corresponding variables in (a) – (c), respectively. As shown in SI Fig. S1, $s = 157.1 \mu\text{m}$ and $40 \mu\text{m}$ for $\phi = 0.52$ and $\phi = 0.23$, respectively.

$a = 0.38 (\pm 0.12)$ for the large pore space ($\phi = 0.52$) and $a = 0.31 (\pm 0.12)$ for $\phi = 0.23$, as shown by the dashed lines in Fig. 6a and b, respectively.

The overall trend of the correlations shows that the greater evaporation rate, the higher salt growth rate. Residual brine evaporates faster in the media with large pore space ($\phi = 0.52$) and results in more salt nucleation. According to our measurements, the water evaporation rate is about $3.9 \times 10^3 \mu\text{m}^2/\text{s}$ on average for the cases of $\phi = 0.52$, which is about 1.73 times than that of $\phi = 0.23$ ($\approx 2.26 \times 10^3 \mu\text{m}^2/\text{s}$) due to the larger air-brine contact area. Therefore, the salt-growing rate is faster on average (by $\approx 33\%$) in the cases of $\phi = 0.52$ ($\approx 1.2 \times 10^3 \mu\text{m}^2/\text{s}$) than those measured from $\phi = 0.23$ ($\approx 0.9 \times 10^3 \mu\text{m}^2/\text{s}$).

To further analyze the correlation between the salt-precipitation rate and brine drying rate for different ϕ , we divided the correlation data (Fig. 6a-b) by their respective interspacing, s ,

between the two pillars and found a good data collapse, shown in Fig. 6c, for different ϕ and initial salt concentrations. Here, the quantity $\dot{V}_{\text{brine}}/(hs)$ physically can represent the receding speed of the residual brine undergoing drying, while $\dot{V}_{\text{salt}}/(hs)$ indicates the speed of local salt precipitation. The well-collapse of our data shown in Fig. 6c reveals a positive and universal correlation with a linear slope of $0.47 (\pm 0.04)$, i.e., implying the salt precipitation speed, $\dot{V}_{\text{salt}}/(hs)$, is about half of Relevant to the CCS in saline formations, this quantitative result would help predict the total amount and the rate of salt precipitation at pore-scale if the brine-drying rate is known or estimated for different porosities.

4 Conclusions

Our microfluidic results reveal the gas-liquid-solid interactions applicable to the CCS processes at pore scales and can offer the following implications for evaluating the effect of salt precipitation at an operational CCS site. First, the three distinct phases of salt precipitation are always observed at pore scales and could be expected during a CCS process. These distinct phases are dependent on the local drying rates of brine, resulting in various size distributions of salt crystals. Second, the positive correlation found, with good data collapse, can be used to relate the speed of salt nucleation with brine drying rate for different porosities. Third, the location of large brine pools plays an essential role in nucleating salt and, hence, the possibility of impairment of the CCS process. From our microfluidic measurements, on the one hand, we notice that small salt crystals precipitate first from the brine trapped in a single-pore area in the first phase, which has an insignificant influence on reducing formation permeability. On the other, in the second fast-drying phase, a large volume of residual brine trapped (close to the outlet) provides an ion source for extended salt nucleation via a self-enhancing mechanism with a capillary flow, providing a positive feedback loop. The extended salt nucleation can reduce the pore connectivity and, hence, hinder the displacement of CO_2 flow during the CCS deployment in deep saline aquifers.

Author contributions

Tsaihsing Martin Ho: Investigation, Formal analysis, Writing - Original Draft, Visualization. **Peichun Amy Tsai:** Conceptualization, Methodology, Validation, Writing - Original Draft, Visualization, Supervision, Funding acquisition.

Conflicts of interest

There are no conflicts to declare.

Acknowledgements

We gratefully acknowledge the support from Canada First Research Excellence Fund (CFREF), Future Energy System (FES) at the University of Alberta, and Canada Foundation for Innovation (NSERC CFI). We also thank S. Bozic and S. Munro for their help with micro-fabrications at the nanoFAB in the University of Alberta. P.A.T. holds a Canada Research Chair in Fluids and Interfaces and gratefully acknowledges funding from the Natural Sciences and Engineering Research Council of Canada (NSERC) and Alberta Innovates.

Notes and references

- 1 S. Bachu and J. Adams, *Energy Convers. Manage.*, 2003, **44**, 3151–3175.
- 2 S. Anderson and R. Newell, *Annu. Rev. Environ. Resour.*, 2004, **29**, 109–142.
- 3 B. Metz, O. Davidson, H. De Coninck, M. Loos and L. Meyer, *IPCC special report on carbon dioxide capture and storage*, 2005.
- 4 K. Michael, A. Golab, V. Shulakova, J. Ennis-King, G. Allinson, S. Sharma and T. Aiken, *Int. J. Greenhouse Gas Control*, 2010, **4**, 659–667.
- 5 D. Y. Leung, G. Caramanna and M. M. Maroto-Valer, *Renewable Sustainable Energy Rev.*, 2014, **39**, 426–443.
- 6 H. E. Huppert and J. A. Neufeld, *Annu. Rev. Fluid Mech.*, 2014, **46**, 255–272.
- 7 M. D. Aminu, S. A. Nabavi, C. A. Rochelle and V. Manovic, *Appl. Energy*, 2017, **208**, 1389–1419.
- 8 C. M. White, B. R. Strazisar, E. J. Granite, J. S. Hoffman and H. W. Pennline, *J. Air Waste Manage. Assoc.*, 2003, **53**, 645–715.
- 9 N. Muller, R. Qi, E. Mackie, K. Pruess and M. J. Blunt, *Energy procedia*, 2009, **1**, 3507–3514.
- 10 S. Grude, M. Landrø and J. Dvorkin, *Int. J. Greenhouse Gas Control*, 2014, **27**, 178–187.
- 11 G. Baumann, J. Henniges and M. De Lucia, *Int. J. Greenhouse Gas Control*, 2014, **28**, 134–146.
- 12 R. Miri and H. Hellevang, *Int. J. Greenhouse Gas Control*, 2016, **51**, 136–147.
- 13 A. Raza, R. Rezaee, R. Gholami, V. Rasouli, C. H. Bing, R. Nagarajan and M. A. Hamid, *J. Nat. Gas Sci. Eng.*, 2015, **26**, 510–517.
- 14 K. Pruess and N. Müller, *Water Resour. Res.*, 2009, **45**, 3.
- 15 K.-Y. Kim, W. S. Han, J. Oh, T. Kim and J.-C. Kim, *Transp. Porous Media*, 2012, **92**, 397–418.
- 16 H. Ott, J. Snippe, K. De Kloe, H. Husain and A. Abri, *Energy Procedia*, 2013, **37**, 3319–3330.
- 17 L. André, Y. Peysson and M. Azaroual, *Int. J. Greenhouse Gas Control*, 2014, **22**, 301–312.
- 18 E. Guyant, W. S. Han, K.-Y. Kim, M.-H. Park and B.-Y. Kim, *Int. J. Greenhouse Gas Control*, 2015, **37**, 299–310.
- 19 J. Oh, K.-Y. Kim, W. S. Han, T. Kim, J.-C. Kim and E. Park, *Adv. Water Resour.*, 2013, **62**, 442–453.
- 20 Y. Peysson, L. André and M. Azaroual, *Int. J. Greenhouse Gas Control*, 2014, **22**, 291–300.
- 21 H. Ott, S. Roels and K. De Kloe, *Int. J. Greenhouse Gas Control*, 2015, **43**, 247–255.
- 22 J. Jeddizahed and B. Rostami, *Adv. Water Resour.*, 2016, **96**, 23–33.
- 23 R. Zhao and J. Cheng, *Greenhouse Gases Sci. Technol.*, 2017, **7**, 624–636.
- 24 C. Zhang, K. Dehoff, N. Hess, M. Oostrom, T. W. Wietsma, A. J. Valocchi, B. W. Fouke and C. J. Werth, *Environ. Sci. Technol.*, 2010, **44**, 7833–7838.
- 25 M. Kim, A. Sell and D. Sinton, *Lab Chip*, 2013, **13**, 2508–2518.
- 26 D. Sinton, *Lab Chip*, 2014, **14**, 3127–3134.
- 27 R. Miri, R. van Noort, P. Aagaard and H. Hellevang, *Int. J. Greenhouse Gas Control*, 2015, **43**, 10–21.
- 28 A. Naillon, P. Joseph and M. Prat, *J. Cryst. Growth*, 2017, **463**, 201–210.
- 29 A. Rufai and J. Crawshaw, *ACS Earth Space Chem.*, 2018, **2**, 320–329.
- 30 M. Nooraiepour, H. Fazeli, R. Miri and H. Hellevang, *Environ. Sci. Technol.*, 2018, **52**, 6050–6060.
- 31 P. Tsai, R. G. Lammertink, M. Wessling and D. Lohse, *Phys. Rev. Lett.*, 2010, **104**, 116102.
- 32 M. D. Abràmoff, P. J. Magalhães and S. J. Ram, *Biophotonics international*, 2004, **11**, 36–42.
- 33 T. Ferreira and W. Rasband, *ImageJ/Fiji*, 2012, **1**, 155–161.
- 34 E. J. Peters, *Live Oak Book Co, Austin, Texas*, 2012.
- 35 D. D. Weis and G. E. Ewing, *J. Geophys. Res. Atmos.*, 1999, **104**, 21275–21285.
- 36 S. Sarig and F. Tartakovsky, *J. Cryst. Growth*, 1975, **28**, 300–305.
- 37 G. V. Chilingar, *Developments in Sedimentology*, Elsevier, 1964, vol. 1, pp. 71–75.
- 38 R. Lenormand, *J. Phys.: Condens. Matter*, 1990, **2**, SA79.